Calibration and Validation of the Menetrey-Willam Constitutive Model for Concrete

Dmitriev, A.[1*], Novozhilov, Yu.[2], Mikhalyuk, D.[3], Lalin, V.[4]

[1] Riga Technical University, Riga, Latvia
[2] LCC CADFEM CIS, St. Petersburg, Russian Federation
[3] Center of Engineering Physics, Simulation and Analysis, JSC, CEO, St. Petersburg, Russian Federation
[4] Peter the Great St. Petersburg Polytechnic University, St. Petersburg, Russian Federation
* dmitriefan@outlook.com

Key words:

Concretes; Calibration; Computer simulation; Constitutive models; Strength; Stress-strain curves; Static loads; Finite element method; Plasticity; ANSYS

Abstract:

Flow plasticity theory has been widely used for nonlinear simulation of reinforced concrete (RC) structures. Constitutive relations of flow plasticity theory in CAE software are referred to as material models. One of the most popular concrete models is the Menetrey-Willam model realized in ANSYS software. The Menetrey-Willam constitutive model can well capture many important mechanical behaviors of concrete such as different tensile and compression strength, nonlinear hardening, softening, and dilatancy. However, there is no published calibration methodology with a clear foundation based on structural design standards. This study suggests an effective calibration procedure to identify the input parameters for the Menetrey-Willam model, mainly according to the CEB-FIP Model Code. Firstly, the identified parameters were verified on basic material tests by a single element simulation. Verification revealed full compliance simulation results with the standards for uniaxial compression, uniaxial tension, and biaxial compression stress states. To validate the ability of the material model to objectively reproduce structural behavior we validated it on six structural tests: confined uniaxial compression of a cube specimen, four-point bending test of a RC beam, three-point bending test of a notched concrete beam, eccentric compression of a RC column, shear rupture test and push-off test of an S-shaped specimen. For all structural tests, a mesh sensitivity analysis was also carried out. The use of the proposed model parameters allows to achieve a good match with the experimental data for all the considered problems almost independently of the mesh size. The obtained parameters can be conveniently used for occasional users without special knowledge in the field of concrete mechanics.

1   Introduction

Concrete is a complex, heterogeneous material that is characterized by nonlinear behavior, various resistance to tension and compression, dilatation under shear distortion, erosion due to both cracking and crushing.

Concrete structures are often analyzed using the finite element method. Currently there are many constitutive models for numerical modeling of concrete behavior. Material models of concrete are usually based on the following theories: theory of plasticity with plastic flow rule [1–4], microplane theory [5–12], endochronic theory [13–16], nonlinear fracture mechanics and damage theory [17–21], theory of visco-plasticity [22]. Each of these theories covers a certain range of concrete behavior, so the choice of an appropriate theory and constitutive model depends on the application specifics.

Most constitutive models for concrete in commercial CAE packages are based on flow plasticity theory. One of the most popular models is the one based on Menetrey–Willam yield surface. This way, there are many papers devoted to the creation of improved constitutive models based on the Menetrey-Willam yield surface [23–32]. However, these models have not been sufficiently validated and are not widely used in CAE software. In the paper [33], the authors proposed the reverse identification of

Menetrey–Willam model parameters, which is implemented in ANSYS software, based on the coincidence of the results of the simulation and the experiment. Obviously, this optimization approach can provide parameters that have no physical foundation and therefore are called into question.

Present study proposes the calibration and validation methodology of the Menetrey-Willam constitutive model for concrete implemented in ANSYS software. In the calibration procedure, all parameters are set according to European standards. Menetrey-Willam constitutive model [1, 3] based on the theory of plasticity with non-associated flow rule. The main components of the model are a loading surface, a function of plastic potential and a formulation of hardening/softening behavior.

2   Methods

2.1   Menetrey-Willam constitutive model

2.1.1   Fundamental constitutive equations and the principal stress space definition

Following the theory of plasticity, the increments of total strain $d\varepsilon$ can be represented as a sum of elastic $d\varepsilon^{el}$ and plastic $d\varepsilon^{pl}$ components:

$$d\varepsilon = d\varepsilon^{el} + d\varepsilon^{pl}.$$

The increment of elastic strain is determined by means of the stress increment through the matrix of elasticity $[D]$, which is determined by elastic modulus E and Poisson's ratio ν (generalized Hooke's law):

$$d\varepsilon^{el} = [D]^{-1} d\sigma.$$

The increment of plastic strain is determined in accordance with the non-associated flow law:

$$d\varepsilon^{pl} = d\lambda \frac{\partial Q}{\partial \sigma},$$

where σ is the stress vector, λ is the non-negative plastic multiplier, Q is the plastic potential function.

The non-associated flow law implies that the direction of the plastic strain vector is oriented along the normal to the surface of the plastic potential Q, which differs from the loading surface function F.

Both loading surface and plastic potential functions are defined as functions of the three stress tensor invariants I_1, J_2, J_3:

$$I_1 = \sigma_1 + \sigma_2 + \sigma_3;$$

$$J_2 = \frac{1}{6}\left[(\sigma_1 - \sigma_2)^2 + (\sigma_2 - \sigma_3)^2 + (\sigma_1 - \sigma_3)^2\right];$$

$$J_3 = \left(\sigma_1 - \frac{I_1}{3}\right)\left(\sigma_2 - \frac{I_1}{3}\right)\left(\sigma_3 - \frac{I_1}{3}\right).$$

For attractive geometric interpretation, the functions are described in Haigh-Westergaard coordinates ξ, ρ, θ, where ξ is the hydrostatic stress invariant, ρ is the deviatoric stress invariant, θ is the deviatoric polar angle. The coordinates depend on principal stress tensor components:

$$\xi = \frac{1}{\sqrt{3}} I_1;$$

$$\rho = \sqrt{2J_2};$$

$$\theta = \frac{1}{3}\arccos\left(\frac{3\sqrt{3}}{2}\frac{J_3}{\sqrt{J_2^3}}\right).$$

2.1.2   Loading surface

The loading surface in Haigh–Westergaard stress space $F(\xi, \rho, \theta)$ is the set of points for which the condition for the beginning of plastic flow is true. Thus, the loading surface separates the zones of elastic and elastic-plastic deformation. Due to hardening and softening, the shape and size of the loading surface are constantly changing.

The Menetrey-Willam constitutive model assumes isotropic hardening in which the loading surface only changes its size while maintaining the coaxiality of the hydrostatic axis.

The loading surface based on Willam-Warnke yield surface [3] and for current stress state is defined by the following function:

$$F\left(\xi,\rho,\theta\right)=\frac{c_2}{c_3}\left[\sqrt{2}\xi+r\rho\right]+\rho^2-\frac{1}{c_3},$$

where

$$r=\frac{4C\cos^2\theta+D^2}{2C\cos\theta+D\sqrt{4C\cos^2\theta+5e^2-4e}},$$

$$C=1-e^2, D=2e-1,$$

$$e=\frac{1+m}{2-m},$$

$$m=\frac{\overline{f}_t}{\overline{f}_{bc}}\frac{f_{bc}^2-\overline{f}_c^2}{\overline{f}_c^2-\overline{f}_t^2}, \tag{2.1}$$

$$c_2=\frac{1}{\sqrt{6}}\left[\frac{1}{\overline{f}_c}-\frac{1}{\overline{f}_{bc}}+\frac{\overline{f}_{bc}-\overline{f}_t}{\overline{f}_c^2}\right], \tag{2.2}$$

$$c_3=\frac{3}{2}\frac{1}{\overline{f}_c^2}. \tag{2.3}$$

In the expressions (2.1)–(2.3) $\overline{f}_c, \overline{f}_t, \overline{f}_{bc}$ are the current uniaxial compressive strength, uniaxial tension strength and biaxial compressive strength, respectively. These values depend on the default values of the strength and compression and tension hardening/softening functions:

$$\overline{f}_t=f_t\Omega_{tc},$$
$$\overline{f}_c=f_c\Omega_c,$$
$$\overline{f}_{bc}=f_{bc}\Omega_c,$$

where

$$\Omega_{tc}=\begin{cases}\Omega_t,\kappa_c\leq\kappa_{cm},\\\Omega_t\Omega_c,\kappa_c>\kappa_{cm},\end{cases}$$

Ω_c and Ω_t are the hardening/softening functions in compression and tension, respectively, κ_c is the current compression–hardening parameter, κ_{cm} is the compression–hardening parameter which corresponds with uniaxial compressive strength. The explanation of these variables is presented below.

2.1.3 Hardening and softening functions

The processes of cracking and crushing are described with a strain–softening model which refers to gradual decrease in strength with additional deformation. This strength reduction may be thought as cohesion decrease or destruction of the microstructure. However, the model is not able to describe the effect of the elastic modulus reduction. It should be considered in the problems where stiffness degradation is important.

The hardening/softening behavior of concrete is modeled by varying the size of the loading surface and the plastic potential surface. The size of these surfaces in the space of principal stresses depends on the current strength values, which are determined by the hardening/softening functions Ω_t and Ω_c as shown above. These functions depend on the compression- and tension-hardening parameters and evolve according to the work hardening expressions [23]:

$$d\kappa_c=\frac{\alpha_c}{\overline{f}_c}\sigma\,d\varepsilon^{pl},$$

$$d\kappa_t=\frac{\alpha_t}{\overline{f}_t}\sigma\,d\varepsilon^{pl},$$

where κ_t is the current tension-hardening parameter, α_c and α_t are the compression and tension weight functions given by the following expressions:

$$\alpha_c = 1 - \alpha_t,$$

$$\alpha_t = \begin{cases} 0, & \tan(\alpha) < -2, \\ \dfrac{1}{1 + \exp(-10\tan\alpha)}, & -2 \le \tan(\alpha) \le 2, \\ 1, & \tan(\alpha) > 2, \end{cases}$$

$$\tan(\alpha) = \sqrt{6}\,\frac{\xi}{\rho}.$$

Note that in the case of simple stress state, the hardening parameter coincides with the value of plastic strain, i.e. $\kappa \equiv \varepsilon^{pl}$.

Menetrey-Willam concrete model realized in ANSYS software can consider linear or exponential softening. Both these approaches meet the requirements of CEB-FIP Model Code [34, 35].

Before any plastic deformation occurs, the hardening function Ω_c holds a constant value of Ω_{ci}, defining the initial loading surface that bounds the initial elastic regime.

In the case of linear softening, the hardening/softening function in compression Ω_c is set of power hardening function and linear softening function (Fig. 2.1).
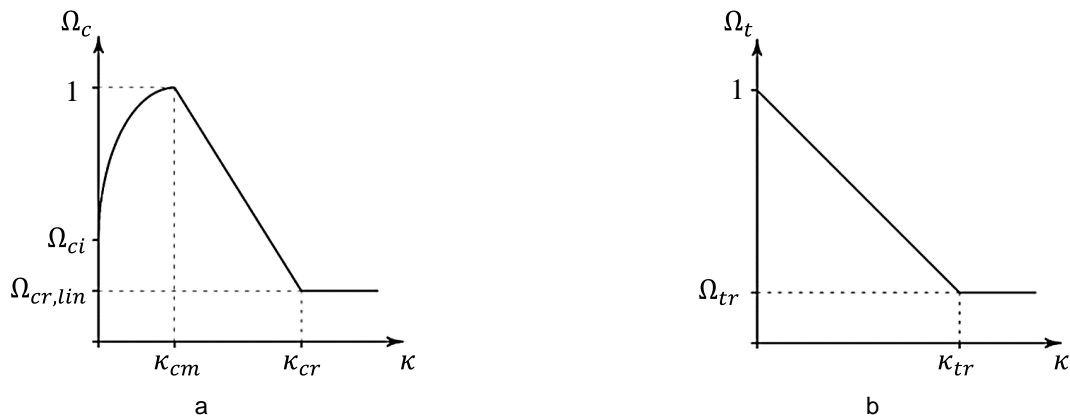

Figure 2.1 – Hardening/softening functions with linear softening: a – in compression; b – in tension

The power hardening function (for $\kappa < \kappa_{cm}$) is:

$$\Omega_c = \Omega_{ci} + (1 - \Omega_{ci}) \cdot \sqrt{2\frac{\kappa_c}{\kappa_{cm}} - \frac{\kappa_c^2}{\kappa_{cm}^2}}. \tag{2.4}$$

At $\kappa_c = \kappa_{cm}$ compressive strength is reached and softening starts. The linear softening function (for $\kappa > \kappa_{cm}$) is:

$$\Omega_c = 1 - \frac{1 - \Omega_{cr}}{\kappa_{cr} - \kappa_{cm}} \cdot (\kappa_c - \kappa_{cm}).$$

The hardening/softening function in tension Ω_t is represented by the linear softening function. So, it is assumed that the behavior of concrete in tension up to the value of f_t is elastic. After reaching f_t the stresses are decreased to the level of residual stress in tension Ω_{tr} that corresponds to the value of equivalent plastic strain κ_{tr}. With further deformation, the material is considered to be completely fractured and is only exhibits a residual frictional strength similar to granular cohesion-less materials.

In the case of exponential softening, the hardening function in compression is the same and is determined by (2.4). Softening behavior is established by set of power and exponential functions

(Fig. 2.2). Plastic strain and corresponding stress in the point of transition from power to exponential softening are labeled as κ_{cu} and Ω_{cu}, respectively.
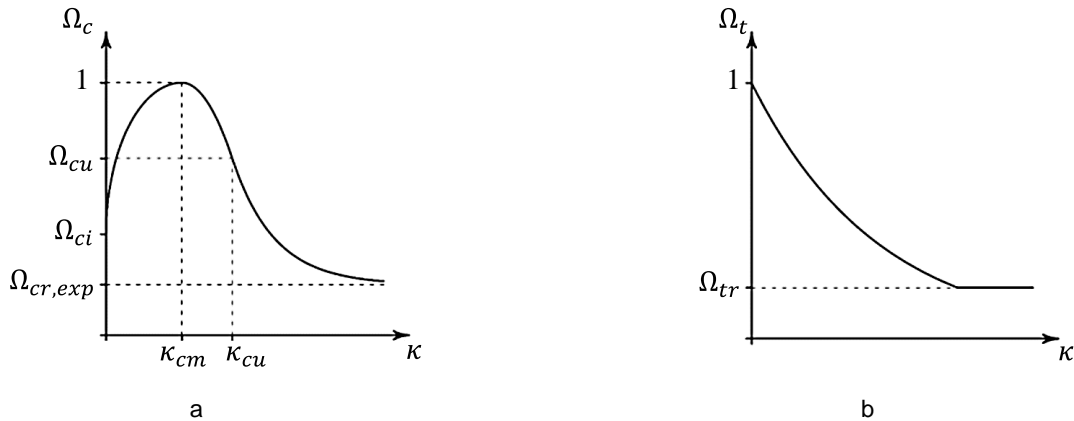

a

b

Figure 2.2 – Hardening/softening functions with exponential softening: a – in compression; b – in tension

The power softening function in compression (for $\kappa_{cm} < \kappa < \kappa_{cu}$) is:

$$\Omega_c = 1 - \left(1 - \Omega_{cu}\right) \cdot \left(\frac{\kappa - \kappa_{cm}}{\kappa_{cu} - \kappa_{cm}}\right)^2.$$

Exponential softening function in compression (for $\kappa > \kappa_{cu}$) is:

$$\Omega_c = \Omega_{cr} + \left(\Omega_{cu} - \Omega_{cr}\right) \cdot \exp\left(2 \frac{\Omega_{cu} - 1}{\kappa_{cu} - \kappa_{cm}} \cdot \frac{\kappa - \kappa_u}{\Omega_{cu} - \Omega_{cr}}\right).$$

Softening behavior in tension is described by the exponential function Ω_t where the volumetric energy dissipated in softening is proportional to the mode I (tensile opening mode) area specific fracture energy in tension G_{ft}:

$$\Omega_t = \exp\left(-\frac{\kappa}{a_t}\right),$$

where

$$a_t = \frac{g_{ft}}{R_t},$$

$$g_{ft} = \max\left(\frac{G_{ft}}{L_i}, \frac{R_t^2}{E}\right).$$

To overcome mesh dependence, the fracture energy is normalized with the effective element length L_i.

2.1.4 Plastic potential function

Dilatancy in concrete, that is characterized by nonlinear volume increase with shear distortion, cannot be correctly described by the associated flow rule [36–40]. The plastic potential function Q, that differs from loading surface function F, determines the direction of the plastic strain vector and leads to the non-associated flow rule.

The plastic potential function defines the non-linear behavior of the material and allows to describe it more accurately. The plastic potential function for current stress state in Haigh-Westergaard coordinates can be written as:

$$Q\left(\xi, \rho\right) = \rho^2 + B_g \rho + C_g \xi,$$

where:

$$B_g = \frac{2\bar{R}_c \tan\psi - \sqrt{2}\,\bar{R}_t}{\sqrt{3}\left(1 - \sqrt{2}\tan\psi\right)},$$

$$C_g = \frac{B_g}{\sqrt{2}} + \frac{2\bar{R}_t}{\sqrt{3}}$$

and ψ is the dilatancy angle.

Both the loading and plastic potential surfaces are not closed in the region of hydrostatic compression; therefore, the constitutive model is unable to reliably describe inelastic response under high compression, close to hydrostatic.

2.2 Validation of the constitutive model

2.2.1 General information about numerical models

Methods and material models used in numerical analysis should be validated by experiments and benchmarks [35, 41, 42]. This validation should include:

1. basic material tests to validate the constitutive relations;
2. structural tests to validate the ability of material model to objectively reproduce structural behavior;
3. mesh sensitivity tests.

For the concrete simulation, 20-node hexahedron elements with quadratic shape function (SOLID186) are used. Behavior and deformation of concrete are defined by the constitutive model described above.

In the models, reinforcement is presented as discrete one-dimensional line elements. Deformation of the rebar is described by the bilinear stress-strain diagram, which involves elastic and yielding stages. Yielding is governed by the second invariant of the deviatoric stress tensor (J2 plasticity). Rebars are modeled by using a 2-nodes beam (BEAM188) or truss (LINK180) finite elements (FE) with linear shape function. Beam FE has both translational and rotational degrees of freedom (DOF); truss FE has only translational DOF.

Interaction between solid and truss meshes occurs via shared nodes with same DOF, so there is a perfect bond between concrete and steel.

The specified displacement is used as a load, which provides a more sustainable solution. The load, which is equivalent to the specified displacement, is calculated as a force reaction in the supports. Also, to overcome convergence difficulties stabilization is used, that means adding artificial damping proportional to pseudo velocity in each node. As shown by the computations, the stabilization energy is negligible compared to strain energy, so the use of artificial stabilization is acceptable.

2.2.2 Basic material tests

Under uniaxial compression (Fig. 2.3), if the relative axial stress doesn't exceed the value Ω_{ci}, the behavior of concrete is elastic. The initiation of hardening behavior with values above Ω_{ci} is associated with the accumulation of microcracks.

Normal concrete behaves almost elastically up to about 30-40% of f_c, so the value $\Omega_{ci} = 0.3\ldots0.4$ is commonly used. To more accurately determine the value of Ω_{ci}, the following formula can be used [32, 33]:

$$\Omega_{ci} = \frac{\sigma_{co}}{f_c} = \frac{f_c^{1.855}}{60 f_c}.$$

The peak strain ε_{c1} at uniaxial compressive strength, following the recommendations [23, 33], can be defined as the minimum of two values:

$$\varepsilon_{c1} = \min \begin{cases} -0.0022, \\ -\dfrac{0.7 f_c^{0.31}}{1000}. \end{cases}$$

Plastic strain at the peak strength point and at the transition point can be calculated as:

$$\varepsilon_{c1}^{pl} \equiv \varepsilon^{pl}(f_c) = \varepsilon_{c1} - \frac{f_c}{E};$$

$$\varepsilon_{c,lim}^{pl} = \varepsilon_{c,lim} - \frac{\sigma_{c,lim}}{E};$$

where $\varepsilon_{c,lim}$ can be taken from Table 2.1 or calculated by the formula [34].

Table 2.1 – $\varepsilon_{c,lim}$ for various concrete grades

Concrete grade	C20	C40	C60	C80
$\varepsilon_{c,lim} \cdot 10^3$	4.2	3.3	2.8	2.4

After the peak strength f_c concrete demonstrates softening behavior which is described by descending part of $\sigma - \varepsilon$ diagram. Note that information about the softening behavior in the standards is almost not presented. The CEB-FIP Model Code recommendations [34] offer two approaches for the description of softening behavior: using linear or polynomial-exponential law. Menetrey-Willam constitutive model is able to cover both techniques.

- • CEB-FIP model with linear softening
- —— Menetrey-Willam with linear softening

a

- • CEB-FIP model with exp. softening
- —— Menetrey-Willam with exp. softening

b
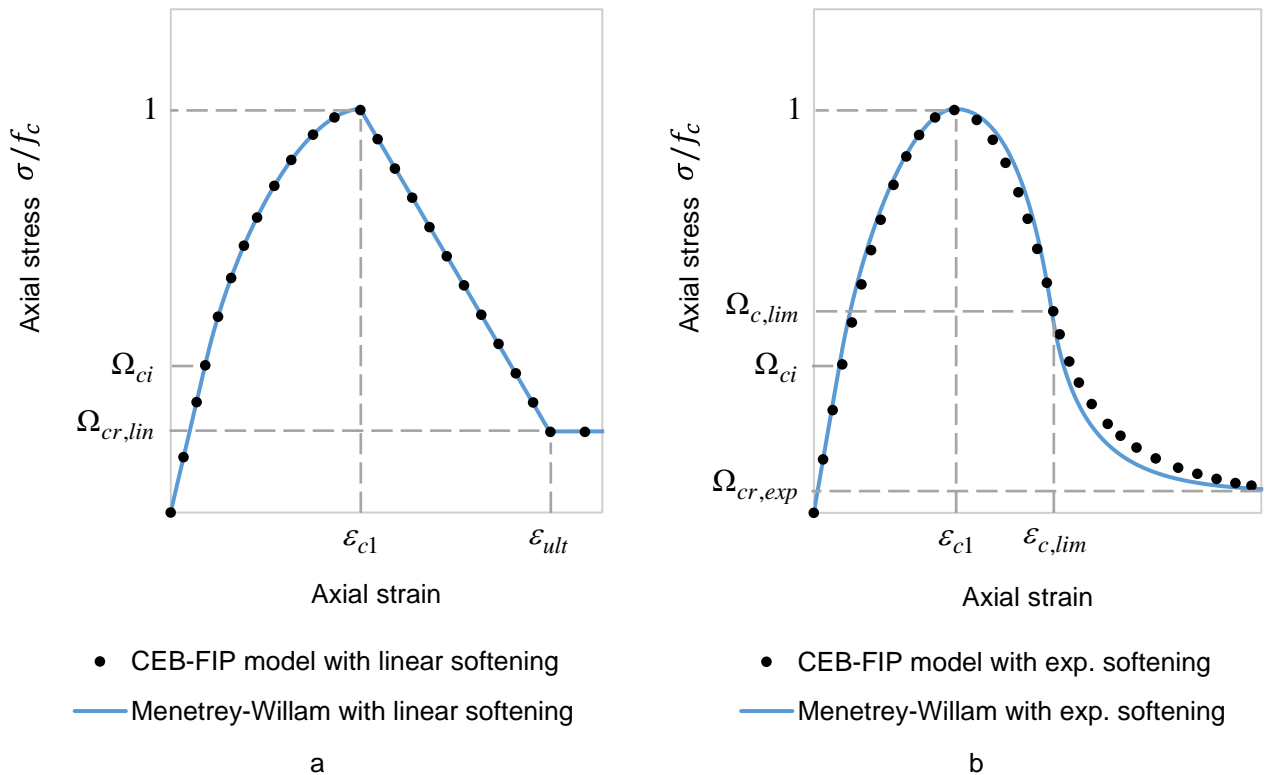
Figure 2.3 – Stress-strain relationship in uniaxial compression: a – with linear softening; b – with exponential softening

For exponential softening there is no information about residual compressive relative stress; based on the diagram from the standards [34] this value is about $\Omega_{cr,exp} = 0.05$. Suitable value of strain at the transition from power law to exponential softening $\Omega_{c,lim}$ is about 0.5…0.7.

Residual compressive relative stress $\Omega_{cr,lin}$ in case with linear softening is equal 0.2 [34]. Ultimate strain in compression ε_{ult} depends on the strength grade of concrete; it can be determined by formula $\varepsilon_{ult} = n \cdot \varepsilon_{c1}$, where n – is constant for certain grade as given in Table 2.2 [34].

Table 2.2 – Coefficient n to describe ultimate strain

Concrete grade	C20	C40	C60	C80
n	3	2	1.5	1.2

In the uniaxial tension test, the behavior of concrete is elastic up to the achievement of tensile strength f_t [34, 43]:

$$f_c \le 50 : f_t = 0.3\left(f_c\right)^{\frac{2}{3}};$$

$$f_c > 50 : f_t = 2.12 \cdot \ln\left(1 + \frac{(f_c + \Delta f)}{10}\right).$$

Post-peak behavior with exponential softening technique is dictated by the yield function in tension Ω_t which depends on the mode I area specific fracture energy in tension G_{ft} given by expression (2.5) and Table 2.3 [34]; with the linear softening descending part of the diagram determined by the limit value of strain in tension κ_{tr} and residual tensile relative stress Ω_{tr}.

$$G_{ft} = G_{ft0}\left(\frac{f_c + 8}{10}\right)^{0.7} \tag{2.5}$$

where G_{ft0} is the base value of the fracture energy, f_c is the uniaxial compressive strength in MPa.

Table 2.3 – Fracture energy values for several concrete grades

Max. aggregate size d_{max}, mm	G_{ft0}, N×m/m^2	G_{ft}, N×m/m^2			
		C20	C40	C60	C80
8	25	50	70	95	115
16	30	60	90	115	135
32	58	80	115	145	175
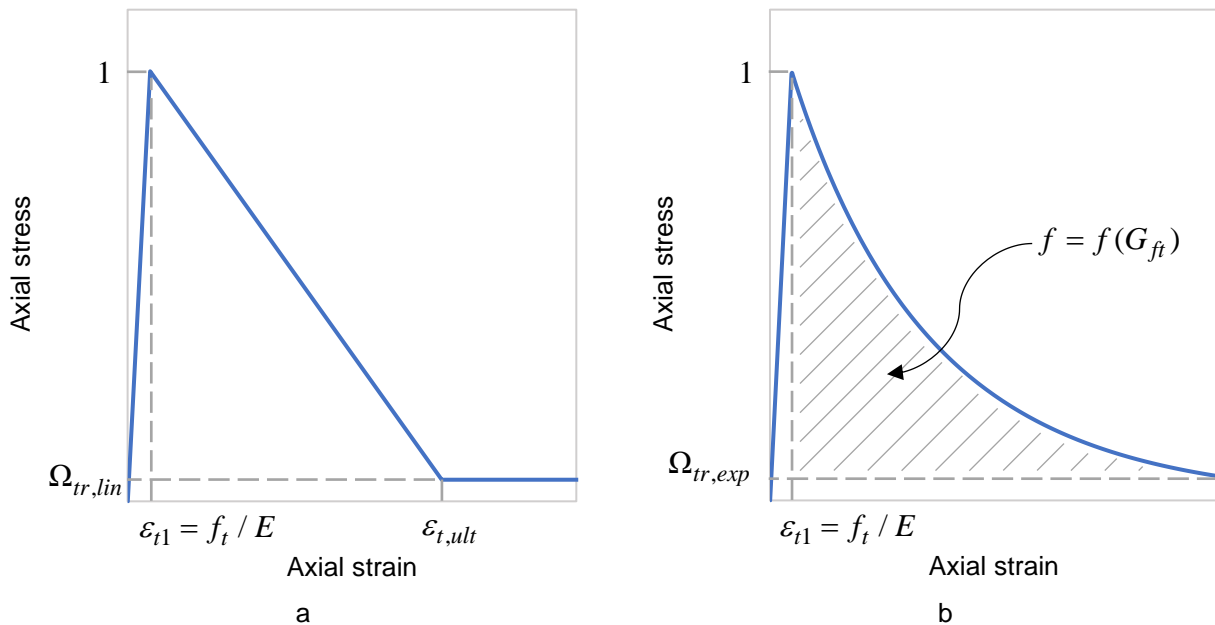
Figure 2.4 – Stress-strain relationship in uniaxial tension

Thus, the fictitious crack in uniaxial tension test is bounded by the two following extreme points:

1. the point where maximal tensile stress reaches f_t;
2. the point where the tensile stress transfer ends and is the beginning of the "stress-free" crack with residual stress value Ω_{tr}.

With a biaxial stressed state, the Menetrey-Willam model is in good agreement with the model adopted in CEB-FIP Model Code 1990 [44]. Here it is considered that biaxial compressive strength $f_{bc} = 1.2 \cdot f_c$ which is well suited for normal strength concrete.
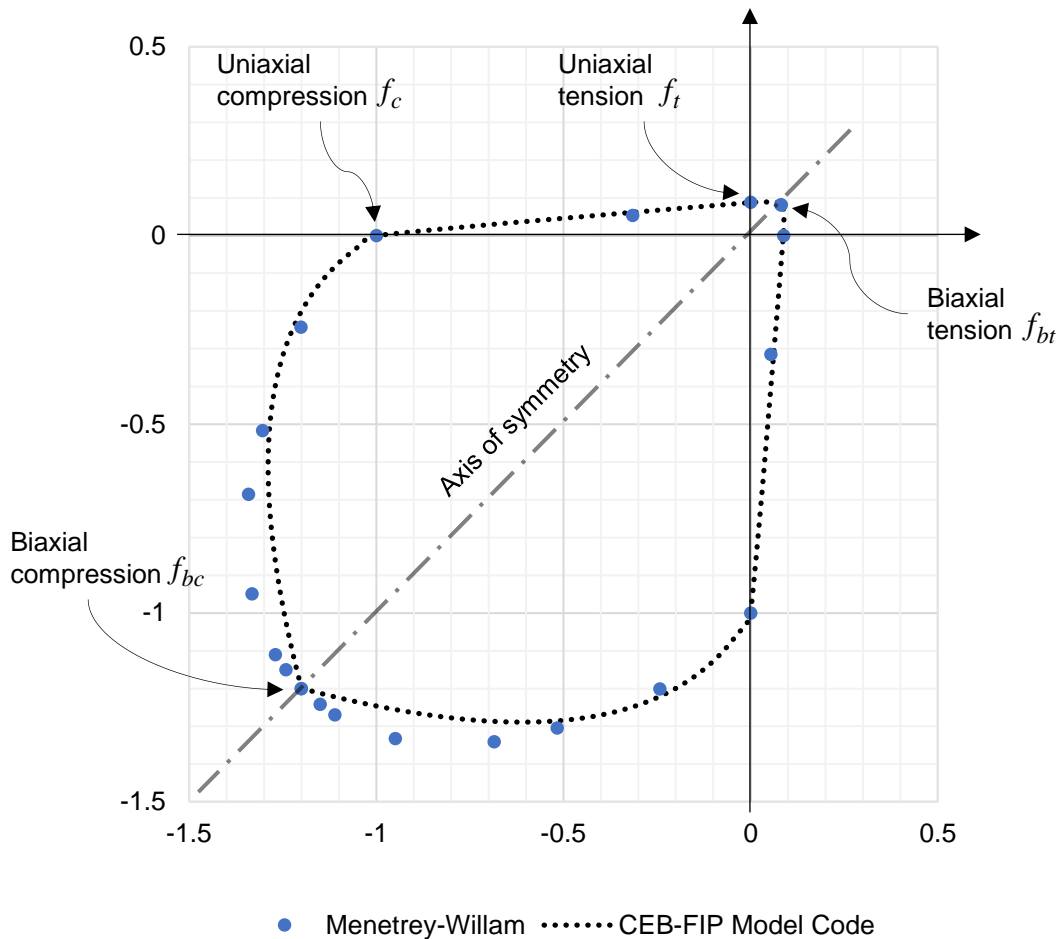
●   Menetrey-Willam   ⋯⋯⋯ CEB-FIP Model Code

Figure 2.5 – Strength of concrete under biaxial stresses

For a more precise definition, biaxial compressive strength f_{bc} can be calculated by the formula [34]:

$$f_{bc} = \left(1.2 - \frac{f_c}{1000} \right) \cdot f_c.$$

One of the important properties of concrete is dilatancy [39, 40]. This property characterizes nonlinear volume increase associated with shear distortion of the material. Dilatation of the concrete is explained by the accumulation of microcracks in the inner structure of the material. Suitable parameter characterizing the dilatant material is the dilatancy angle. The physical interpretation of ψ can be demonstrated by a shear box test (Fig. 2.6).
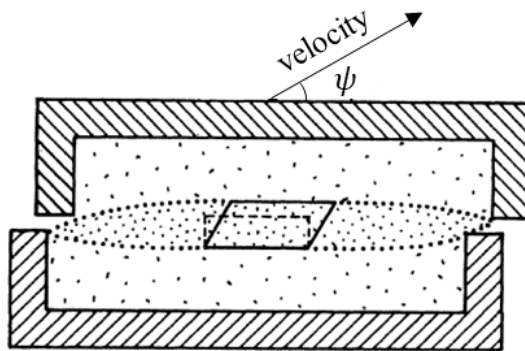
Figure 2.6 – Shear box test showing the effect of dilatancy

In this test, the dilatancy angle should be considered as the uplift angle in a shear band [36]. Typical values of ψ for concrete are $8°…15°$ [39, 40].

3 Results and discussion

3.1 Structural tests

3.1.1 Confined uniaxial compression

The first structural example is uniaxial compression of the cube with friction. The grade of concrete C40 is investigated. Data about the strength of confined cube is presented in the standards [34, 43]; for the grade of concrete C40, cube strength is 50 MPa.

It is known that concrete cubes in material tests have higher strength than cylinders due to the smaller height and the greater influence of friction between concrete faces and steel plates. Due to friction, cracking is restrained, and specimen can carry higher loads.

The geometry, boundary conditions and loading setup are shown in Fig. 3.1. Since the geometry has two planes of symmetry, only one quarter is modeled. The modeling is conducted with three meshes: coarse (592 DOF), medium (14695 DOF), fine (42669 DOF).
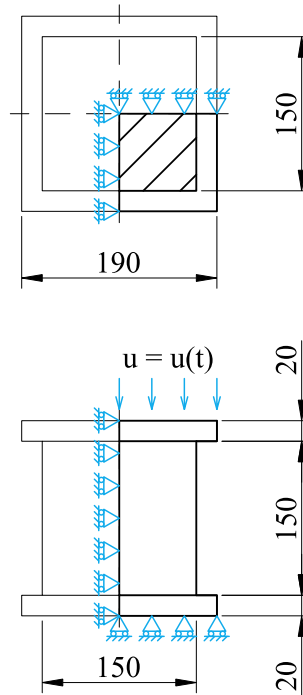

Figure 3.1 – Details of the concrete cube model

The input parameters for concrete C40 are presented in Table 3.1. The friction coefficient between the concrete specimen and steel plates is equal 0.40 [45].

Table 3.1 – Input parameters of Menetrey-Willam material model for concrete C40

Parameter	Value
Young's modulus E , MPa	36500
Poisson's ratio v	0.2
Uniaxial compressive strength f_c , MPa	40
Uniaxial tensile strength f_t , MPa	3.5
Biaxial compressive strength f_{bc} , MPa	46.4
Dilatancy angle ψ , °	9
Plastic strain at uniaxial compressive strength ε_{c1}^{pl}	0.001104
Plastic strain at the transition from power law to exponential softening $\varepsilon_{c,lim}^{pl}$	0.003177
Relative stress at the start of nonlinear hardening Ω_{ci}	0.4
Residual relative stress at the point of transition $\Omega_{c,lim}$	0.5
Residual compressive relative stress Ω_{cr}	0.05

Residual tensile relative stress Ω_{tr}	0.05
Mode I area-specific fracture energy G_{ft} , N·m/m²	90

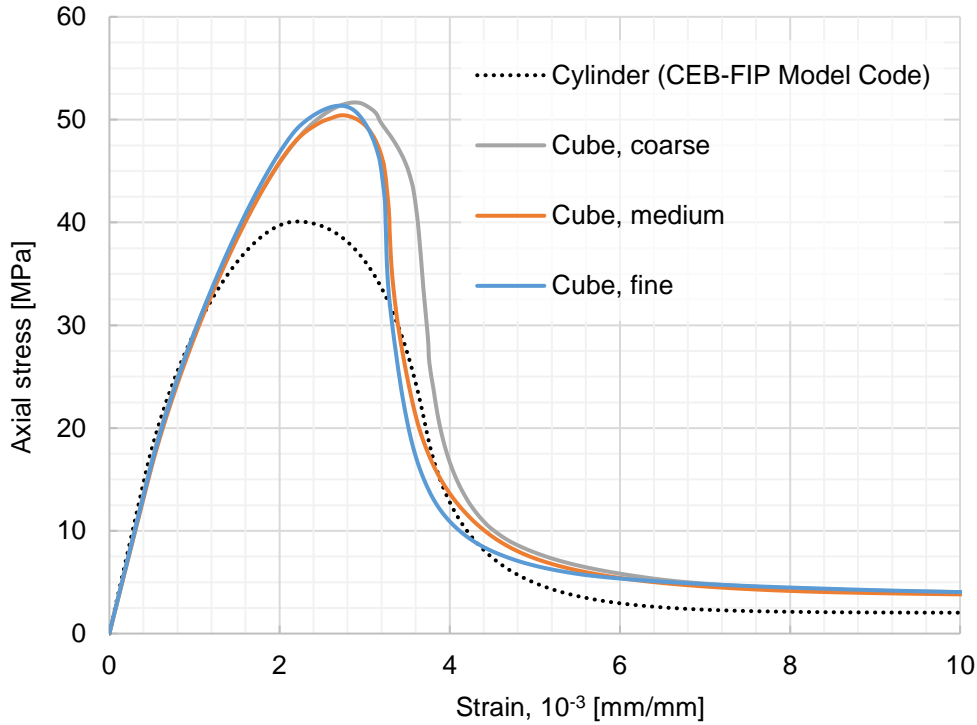The global responses of analyses for a confined cube and cylinder are presented in Fig. 3.2.

Figure 3.2 – Stress-strain relationship for cube and cylinder in compression with friction

Modeling results are presented in Table 3.2. Errors in the last column are calculated as

$$\Delta = \frac{Modeling - Reference}{Reference} \cdot 100\%.$$

Table 3.2 – Results for confined compression of cube

Criteria	Ref.	Mesh	Model	Error, %
Cube strength, kN	50	Coarse	51.68	3.36
		Medium	50.44	0.88
		Fine	51.36	2.72

Numerical model can describe the increase of compressive strength and peak strain which is the result of the action of friction on specimens of different geometric shapes.

The obtained compressive strength (is about 51 MPa) is in good agreement with data from the standards and does not depend on mesh size.

3.1.2 Four-point bending test of a RC beam

The second structural example is a four-point bending test of a reinforced concrete beam reported in [46]. The geometry, boundary conditions and loading setup are shown in Fig. 3.3. Since the geometry has two planes of symmetry, only one quarter is modeled. The modeling is conducted with three meshes: coarse (6661 DOF), medium (19499 DOF), fine (54963 DOF).
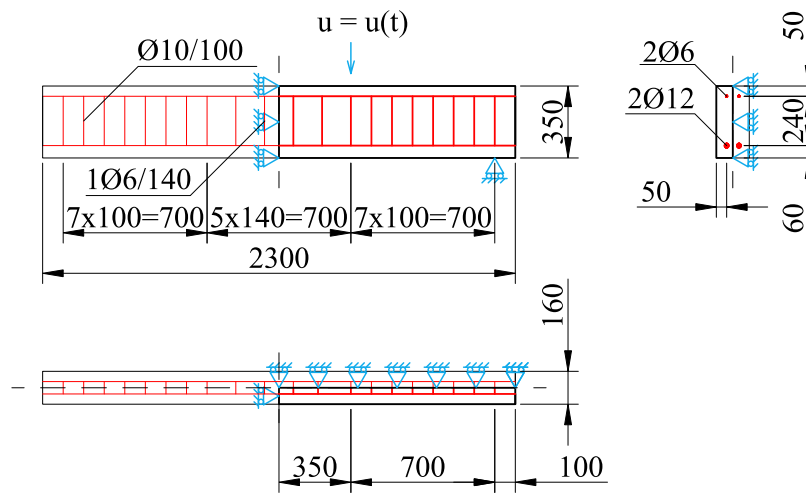
Figure 3.3 – Details of RC beam model

The input parameters for concrete are chosen as $E = 30000$ MPa, $v = 0.18$, $f_c = 35$ MPa, $f_t = 3.2$ MPa, $f_{bc} = 40.8$ MPa, $\varepsilon_{c1} = 0.0022$, $\varepsilon_{c,lim} = 0.0037$, $G_f = 70$ N·m/m². All other parameters are set to their default values described in table 3.1.

Table 3.3 – Input parameters of elastoplastic material model for steel rebars

Parameter	Value
Young's modulus E [MPa]	200000
Poisson's ratio v	0.3
Yield stress $\sigma_y\left(\varnothing12\right)$ [MPa]	650
Yield stress $\sigma_y\left(\varnothing6\right)$ [MPa]	330

The global responses of analyses and experimental results are compared in the form of load-deflection curves presented in Fig. 3.4.
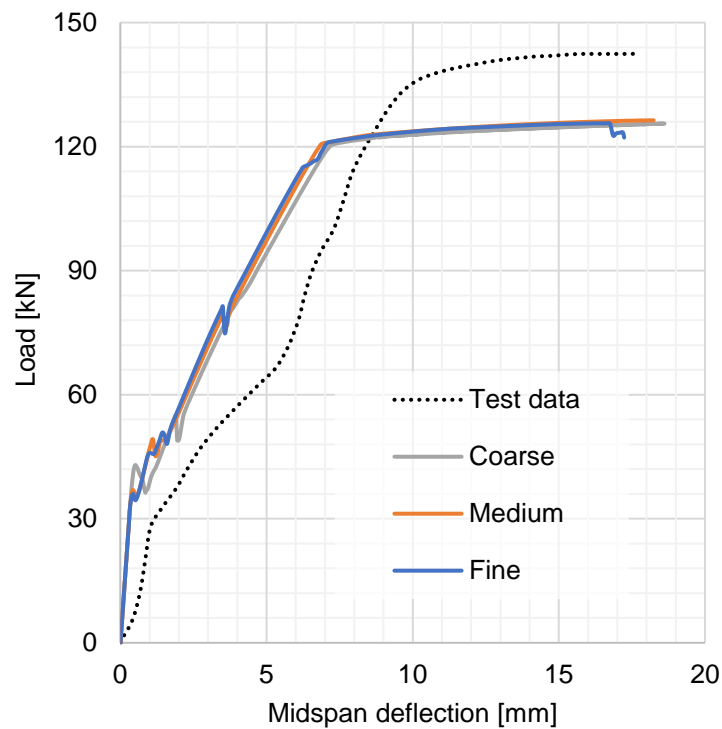

Figure 3.4 – Load-displacement curves for four-point bending test of RC beam

Modeling results are presented in 3.4.

Table 3.4 – Results for four-point bending test of RC beam

Dmitriev, A., Novozhilov, Yu., Mikhalyuk, D., Lalin, V.,
Calibration and Validation of the Menetrey-Willam Constitutive Model for Concrete; 2020; *Construction of Unique Buildings and Structures;* Volume **88** Article No 8804. doi:10.18720/CUBS.88.4

Criteria	Ref.	Mesh	Model	Error, %
Load capacity, kN	140.10	Coarse	123.76	11.66
		Medium	124.76	10.95
		Fine	124.68	11.01
Cracking load, kN	35.20	Coarse	37.35	6.11
		Medium	33.51	4.80
		Fine	34.46	2.10

Average calculated load capacity is about 124.4 kN, which is 11.21% lower than the experimental data (140.1 kN). Note that the ultimate load obtained by the authors with according to standard ACI 440-2R-08 is 125 kN and differs from the modeling result by 0.6%.

During the experiment, the load corresponding to the appearance of the first crack P_{cr} =35.2 kN was also observed. The appearance of a crack in the simulation corresponds to the break point of the curve when the rigidity of the system begins to fall due to the accumulation of significant plastic strain. Thus, the average calculated load at which the crack appears is 35.1 kN and differs from the experimental results by 0.3%.

In general, the response of the system in modeling is more rigid than in the experiment. This can be explained by the existence of microcracks and imperfections of the specimen, which are not considered by the model. Note also that the structural response obtained with the model is mesh independent.

3.1.3 Three-point bending test of a notched concrete beam

The third structural example is a three-point bending test of a notched beam reported in [47].

The beam is made of plain concrete and has no reinforcement. The geometry, boundary conditions and loading setup are shown in Fig. 3.5. Since the geometry has two planes of symmetry, only one quarter is modeled. The modeling is conducted with three meshes with a different number of segments above the notch: coarse with 2 segments (3334 DOF), medium with 3 segments (9432 DOF), fine with 4 segments (40469 DOF).
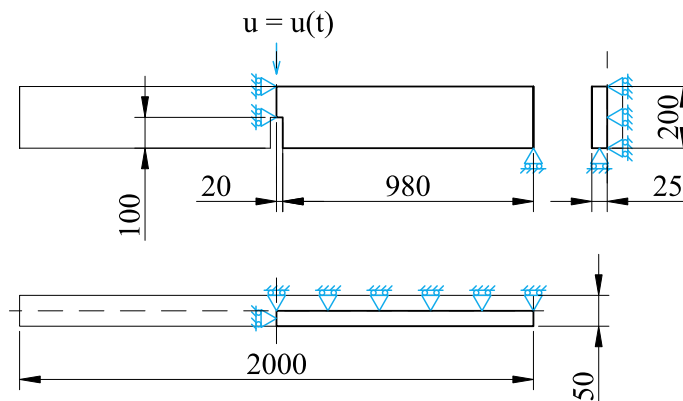

Figure 3.5 – Details of the plain concrete beam model

The input parameters are chosen as $E = 36500$ MPa, $v = 0.20$, $f_c = 40$ MPa, $f_t = 3.33$ MPa, $f_{bc} = 46.4$ MPa, $\varepsilon_{c1} = 0.0022$, $\varepsilon_{c,lim} = 0.0037$, $G_f = 124$ N·m/m². All other parameters are set to their default values described in Table 3.1.

The global responses of analyses and experimental results are compared in the form of load-deflection curves presented in Fig. 3.6.
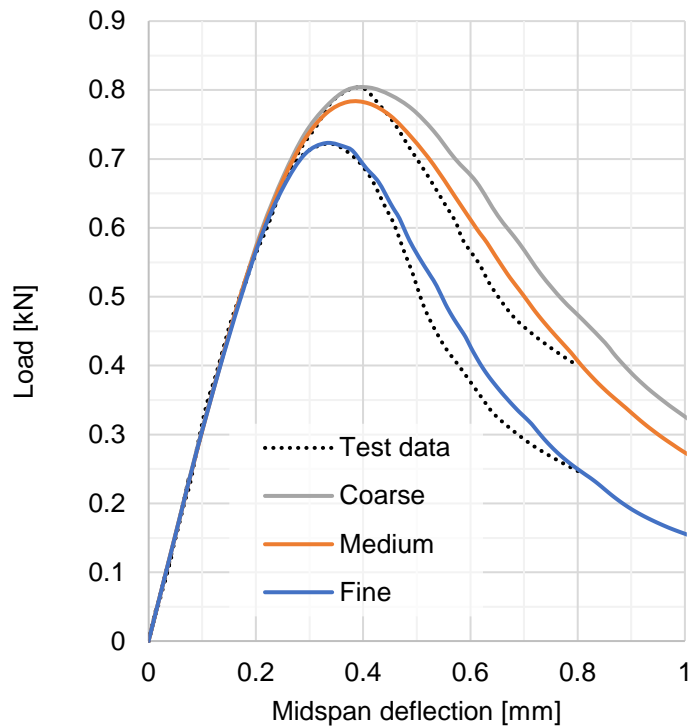
Figure 3.6 – Load-displacement curves for three-point bending test of the notched beam

Modeling results are presented in Table 3.5.

Table 3.5 – Results for three-point bending test of the notched beam

Criteria	Ref. (aver.)	Mesh	Model	Error, %
Load capacity, N	762.96	Coarse	803.68	5.34
		Medium	782.60	2.57
		Fine	723.24	5.21
Peak deflection, mm	0.369	Coarse	0.411	11.38
		Medium	0.371	0.54
		Fine	0.331	10.30

The results of the experiments are different due to the effect of concrete heterogeneity and location of aggregate particles on tensile strength and fracture energy. Peak load and deflection for the upper test curve is 804.14 N and 0.395 mm, respectively; for lower curve is 721.78 N and 0.343 mm.

The simulation results correlate well with the range of the experimental data: peak load varies from 723.24 N to 803.68 N, midspan deflection varies from 0.331 mm to 0.411 mm. Postfailure behavior corresponds to the experimental data too. Note that mesh size influences the results but within the range of the test data.

3.1.4 Eccentric compression of a RC column

The fourth structural example is compression of a reinforced concrete column subjected to a compressive force reported in [48]. The force acts with an eccentricity equal to 1/10 of the cross-sectional width. In the reference article, many experiments with various transversal reinforcement and concrete grades are presented. Here only one case with the distance between transversal rebars equal to 50 mm is considered.

The geometry, boundary conditions and loading setup are shown in Fig. 3.3. Since the geometry has a plane of symmetry, only one-half is modeled. The modeling is conducted with three meshes: coarse (14598 DOF), medium (29995 DOF), fine (73153 DOF).
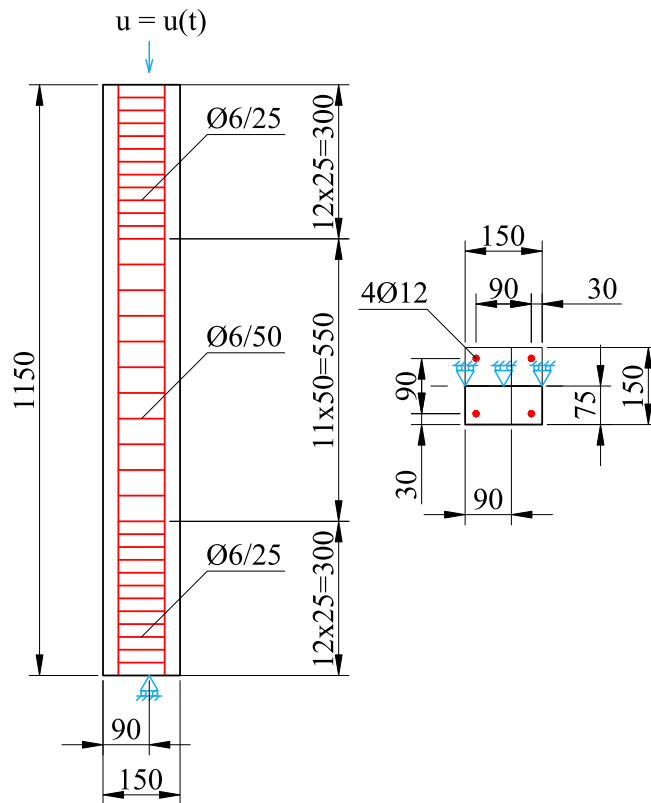
Figure 3.7 – Details of RC column

The concrete properties are defined from the uniaxial compression test (Fig. 3.8). Linear softening is used to describe post-peak behavior. The input parameters are chosen as $E = 30000$ MPa, $\nu = 0.20$, $f_c = 30$ MPa, $f_t = 2.4$ MPa, $f_{bc} = 35$ MPa, $\varepsilon_{c1} = 2.47 \cdot 10^{-3}$, $\varepsilon_{ult} = 0.0151$, $\Omega_{ci} = 0.7$, $f_y(\varnothing 12) = 560$ MPa, $f_y(\varnothing 6) = 310$ MPa. All other parameters are set to their default values described in Table 3.1, 3.3.
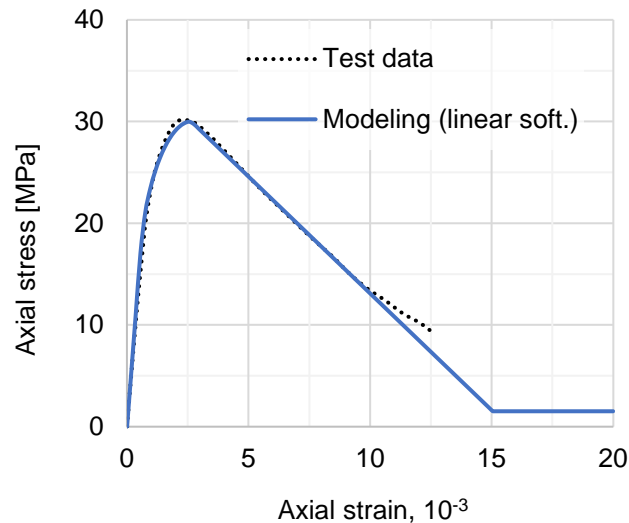

Figure 3.8 – Uniaxial compression test performed in [39]

In this example one feature is detected. The solver cannot obtain the numerical solution of the post-peak response with LINK180 finite elements. For reinforcement modeling in this problem element BEAM188 is used with bending and shear stiffnesses because it provides more sustainable solution after failure.

In the experiments the lateral deflection value in the middle of the column height is measured. The global responses of analyses and experimental results are compared in the form of load-deflection curves presented in Fig. 3.9.
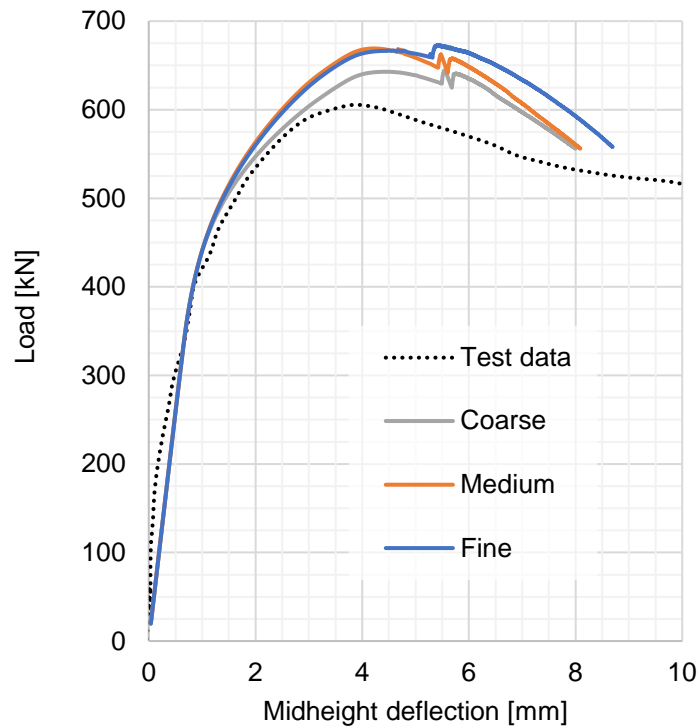
Figure 3.9 – Load-displacement curves for compression of RC column

From a series of experiments, it was obtained that the peak force is 617.6±18.7 kN and peak midheight deflection is 3.84±0.18 mm.

Modeling results are presented in Table 3.6. In the modeling the obtained average load capacity value is 659.7 kN and the deflection is 4.43 mm; the error with the mean experimental values is about 7% and 15%, respectively. After the deflection is equal to 8 mm, the solver cannot obtain the solution since all reinforcement is yielded and the concrete is completely failed in the compression side.

Table 3.6 – Results for RC column compression

Criteria	Ref. (aver.)	Mesh	Model	Error, %
Load capacity, kN	617.60	Coarse	669.16	8.35
		Medium	642.96	4.11
		Fine	666.98	8.00
Midheight deflection, mm	3.84	Coarse	4.21	9.64
		Medium	4.42	15.10
		Fine	4.67	21.61

Overall, the modeling describes the deformation with good accuracy but slightly overestimates the ultimate load and deflection.

3.1.5 Shear rupture test

The fifth structural example is the shear rupture test reported in [49]. The objective of the test is to create a zone of pure shear stress state in a concrete specimen which is under compression as shown in Fig. 3.10.
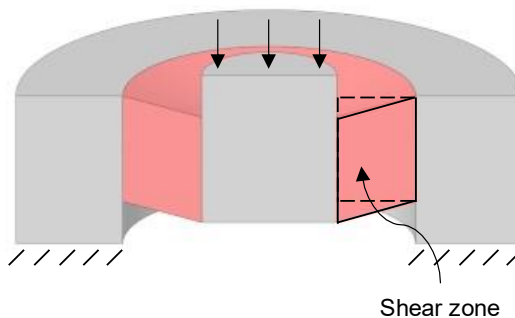

Shear zone

Figure 3.10 – Formation of a pure shear zone in the specimen

The geometry, boundary conditions and loading setup are shown in Fig. 3.11. Despite that the geometry is an axisymmetric, a full-size model was created. The modeling is conducted with three meshes: coarse (24124 DOF), medium (39756 DOF), fine (167997 DOF).
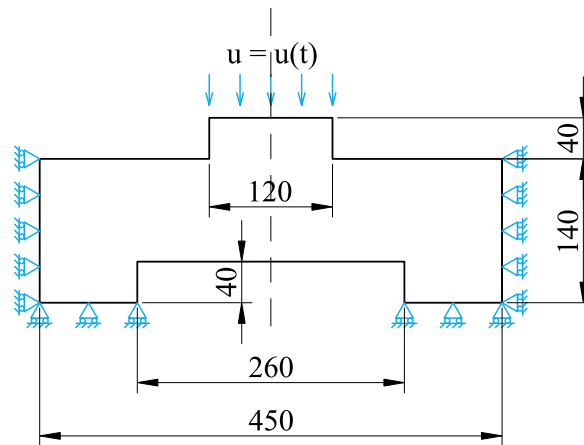

Figure 3.11 – Details of rupture concrete specimen

The input parameters are chosen as $E = 20000$ MPa, $v = 0.2$, $f_c = 20$ MPa, $f_t = 1.2$ MPa, $f_{bc} = 23.6$ MPa, $\varepsilon_{c1} = 0.0022$, $\varepsilon_{c,lim} = 0.0042$, $G_f = 50$ N·m/m², $\Omega_{ci} = 0.216$. All other parameters are set to their default values described in Table 3.1.

The global responses of analyses and experimental results are compared in the form of load-displacement curves presented in Fig. 3.12.
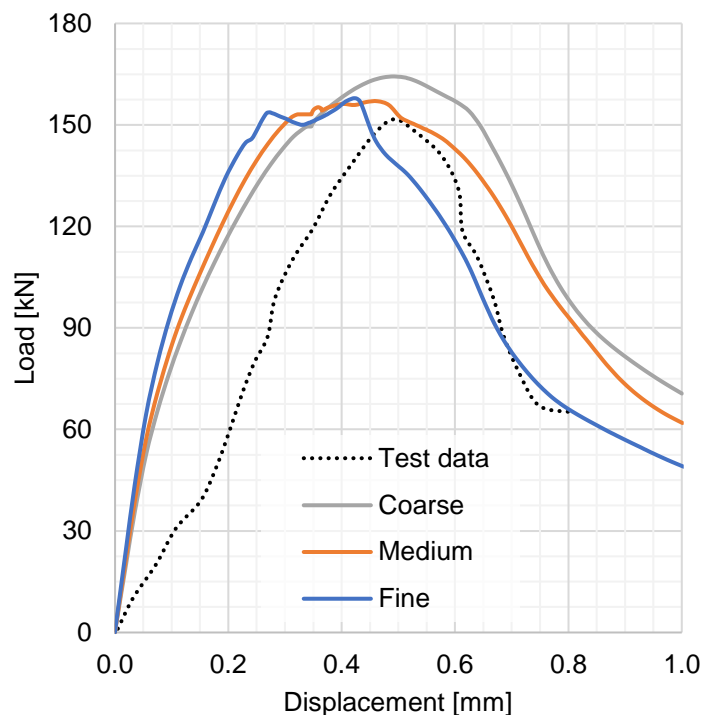

Figure 3.12 – Load-displacement curves for a shear rupture test

Modeling results are presented in Table 3.7. The simulation showed good agreement with the experiment: the peak load is 5% higher; the peak displacement is 7% lower.

Dmitriev, A., Novozhilov, Yu., Mikhalyuk, D., Lalin, V.,
Calibration and Validation of the Menetrey-Willam Constitutive Model for Concrete; 2020; *Construction of Unique Buildings and Structures;* Volume **88** Article No 8804. doi:10.18720/CUBS.88.4

Table 3.7 – Results for the shear rupture test

Criteria	Ref.	Mesh	Model	Error, %
Peak load, kN	151.76	Coarse	164.37	8.31
		Medium	157.08	3.51
		Fine	157.96	4.09
Peak deflection, mm	0.495	Coarse	0.493	0.40
		Medium	0.464	5.88
		Fine	0.422	14.40

The more rigid response of the system in modeling is probably caused by the lack of initial data (only cylindrical strength is given in [49]) and possible initial microdamage in the specimen. Besides, some discrepancy is in the boundary conditions: in the simulation, the outer surface of the sample is fixed from radial and vertical displacement; while in the experiment, there is some flexibility in the radial and vertical directions.

3.1.6 Push-off test of an S-shaped specimen

The sixth structural example is the push-off test of the S-shaped RC specimen reported in [50]. The push-off specimen was first developed by Mattock and Hawkins [51] to investigate the relationships between material, geometric properties and shear strength. As a result of these investigations an empirical Hawkins model was developed and then was improved [51].

In the specimen subjected to compression a direct shear plane is formed (Fig. 3.13). Since whole compressive pressure is transmitted through the shear plane, so the average shear stress τ_a is obtained by dividing the force reaction R_v by the vertical plane area bd : $\tau_a = R_v / bd$.

The geometry, boundary conditions and loading setup are shown in Fig. 3.13. The modeling is conducted with three meshes: coarse (8547 DOF), medium (25804 DOF), fine (78244 DOF).
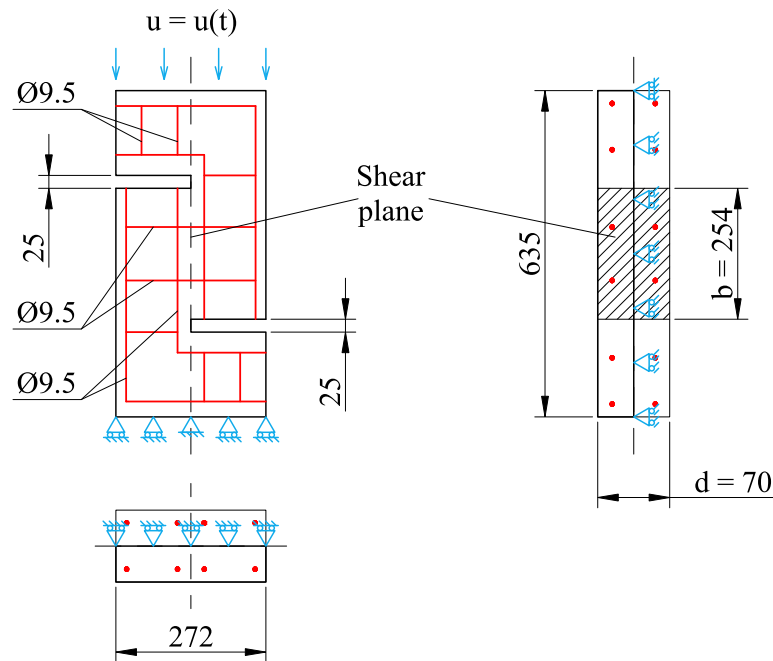

Figure 3.13 – Details of S-shaped specimen

The input parameters are chosen as $E = 20000$ MPa, $v = 0.24$, $f_c = 37.6$ MPa, $f_t = 2.4$ MPa, $f_{bc} = 43.71$ MPa, $\varepsilon_{c1} = 0.0022$, $\varepsilon_{c,lim} = 0.0041$, $G_f = 120$ N·m/m², $\Omega_{ci} = 0.4$. All other parameters are set to their default values described in Table 3.1.

The global responses of analyses and experimental results are compared in the form of average shear stress-slip curves presented in Fig. 3.14.
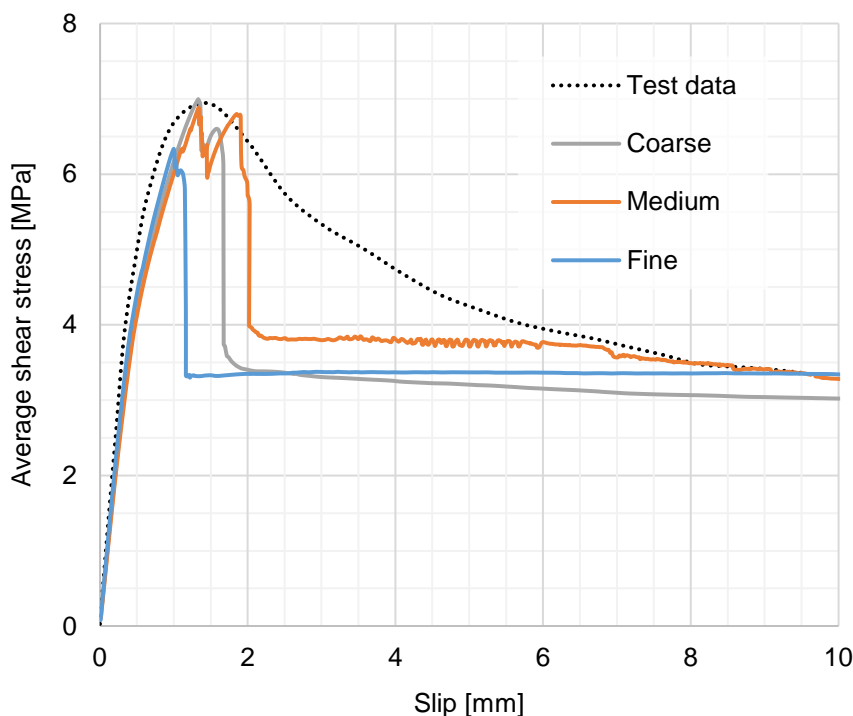
Figure 3.14 – Stress-slip relationship for push-off test

In the experiment, decreasing shear stress is slow, whereas in the simulation stress decreases suddenly since concrete has completely lost its strength and rebars yield. Modeling results are presented in table 3.8.

Table 3.8 – Results for push-off test

Criteria	Ref.	Mesh	Model	Error, %
Max. shear stress, MPa	6.94	Coarse	7.00	0.86
		Medium	6.88	0.86
		Fine	6.39	7.93
Peak deflection, mm	1.48	Coarse	1.33	10.14
		Medium	1.33	10.14
		Fine	1.00	32.43
Residual shear stress, MPa	3.35	Coarse	3.02	9.85
		Medium	3.28	2.09
		Fine	3.34	0.30

Shear stress calculated based on simulation matches experimental data well enough: both maximum and residual shear stress has average errors about 3%. Peak slip is less consistent with the experiment: average error is 18%.

4   Conclusions

The Menetrey-Willam model is an advanced constitutive model for concrete where the loading surface depends on three invariants of stress tensor, hardening and softening functions, plastic potential function. Despite strong theoretical and experimental background, the model contains some parameters which limit its wide applicability. So, a method of model calibration and setup for concrete was presented in this study. Most of the model parameters were taken directly from the CEB-FIP Model Code.

The proposed method has been further verified on basic material tests by a single element simulation. Full compliance of the simulation results with the standards for some stress states is shown.

Finally, the method was validated based on six tests with plain and reinforced concrete structures. The results showed that the Menetrey-Willam constitutive model with the proposed parameters can predict stress-strain state with good accuracy.

5   Acknowledgements

References

1. Menetrey, P.H., Willam, K.J. Triaxial failure criterion for concrete and its generalization. ACI Structural Journal. 1995. 92. Pp. 311–318.
2. Ottosen, N.S. A Failure Criterion for Concrete. ASCE Engineering Mechanics Division. 1977. 103(4). Pp. 527–535.
3. Willam, K.J., Warnke, E.P. Constitutive model for triaxial behaviour of concrete. International Association for Bridges and Structural Engineering. 1974. 19. Pp. 1–30. DOI:10.5169/seals-17526.
4. Grassl, P., Lundgren, K., Gylltoft, K. Concrete in compression: a plasticity theory with a novel hardening law. International Journal of Solids and Structures. 2002. 39(20). Pp. 5205–5223. DOI:10.1016/S0020-7683(02)00408-0. https://www.sciencedirect.com/science/article/pii/S0020768302004080.
5. Bažant, Z.P., Yuyin, X., Prat, P.C. Microplane Model for Concrete. I: Stress-Strain Boundaries and Finite Strain. Journal of Engineering Mechanics. 1996. 122(3). Pp. 245–254. DOI:10.1061/(ASCE)0733-9399(1996)122:3(245).
6. Bažant, Z.P., Xiang, Y., Adley, M.D., Prat, P.C., Akers, S.A. Microplane Model for Concrete: II: Data Delocalization and Verification. Journal of Engineering Mechanics. 1996. 122(3). Pp. 255–262. DOI:10.1061/(ASCE)0733-9399(1996)122:3(255).
7. Bazant, Z.P., Ozbolt, J. Non local microplane model for fracture, damage and size effects in structures. J. Engrg. Mech., ASCE. 1990. 116(11). Pp. 2485–2505. DOI:10.1061/(ASCE)0733-9399(1990)116:11(2485).
8. Bazant, Z.P., Ozbolt, J. Compression Failure of Quasibrittle Material: Nonlocal Microplane Model. Journal of Engineering Mechanics. 1992. 118(3). Pp. 540–556. DOI:10.1061/(ASCE)0733-9399(1992)118:3(540).
9. Bažant, Z.P., Prat, P.C. Microplane Model for Brittle-Plastic Material: I. Theory. Journal of Engineering Mechanics. 1988. 114(10). Pp. 1672–1688. DOI:10.1061/(ASCE)0733-9399(1988)114:10(1672).
10. Bažant, Z.P., Prat, P.C. Microplane Model for Brittle-Plastic Material: II. Verification. Journal of Engineering Mechanics. 1988. 114(10). Pp. 1689–1702. DOI:10.1061/(ASCE)0733-9399(1988)114:10(1689).
11. Bažant, Z.P., Byung, H.O. Microplane Model for Progressive Fracture of Concrete and Rock. Journal of Engineering Mechanics. 1985. 111(4). Pp. 559–582. DOI:10.1061/(ASCE)0733-9399(1985)111:4(559).
12. Bažant, Z.P., Gambarova, P.G. Crack Shear in Concrete: Crack Band Microflane Model. Journal of Structural Engineering. 1984. 110(9). Pp. 2015–2035. DOI:10.1061/(ASCE)0733-9445(1984)110:9(2015).
13. Valanis, K.C., Read, H.E. An endochronic plasticity theory for concrete. Mechanics of Materials. 1986. 5(3). Pp. 277–295. DOI:10.1016/0167-6636(86)90024-4. https://www.sciencedirect.com/science/article/pii/0167663686900244?via%3Dihub.
14. Bazant, Z.P., Bhat, P.D., Shieh, C.L. Endochronic theory for inelasticity and failure analysis of concrete structuresUnited States, 1976.
15. Bažant, Z.P. Endochronic inelasticity and incremental plasticity. International Journal of Solids and Structures. 1978. 14(9). Pp. 691–714. DOI:10.1016/0020-7683(78)90029-X. https://www.sciencedirect.com/science/article/pii/002076837890029X?via%3Dihub.
16. Bažant, Z.P., Ching-Long Shieh. Endochronic model for nonlinear triaxial behavior of concrete. Nuclear Engineering and Design. 1978. 47(2). Pp. 305–315. DOI:10.1016/0029-5493(78)90074-2. https://www.sciencedirect.com/science/article/pii/0029549378900742?via%3Dihub.
17. Kachanov, L.M. Introduction to Continuum Damage Mechanics. Springer, Dordrecht, 1986.

18. Krajcinovic, D., Fonseka, G.U. The Continuous Damage Theory of Brittle Materials, Part 1: General Theory. Journal of Applied Mechanics. 1981. 48(4). Pp. 809–815. DOI:10.1115/1.3157739.

19. Krajcinovic, D. Constitutive Equations for Damaging Materials. Journal of Applied Mechanics. 1983. 50(2). Pp. 355–360. DOI:10.1115/1.3167044.

20. Krajcinovic, D., Mastilovic, S. Some fundamental issues of damage mechanics. Mechanics of Materials. 1995. 21(3). Pp. 217–230. DOI:10.1016/0167-6636(95)00010-0. https://www.sciencedirect.com/science/article/pii/0167663695000100.

21. Krajcinovic, D. Damage Mechanics. Mechanics of Materials. 1989. 8 (2-3). Pp. 117–197. DOI: 10.1016/0167-6636(89)90011-2.

22. Valanis, K. A Theory of Viscoplasticity without a Yield Surface. Part 1. General Theory. Archives of Mechanics. 1970. 23. Pp. 517–551.

23. Pisano, A.A. An algorithmic approach for peak load evaluation of structural elements obeying a Menetrey-Willam type yield criterion. Electronic Journal of Differential Equations. 2012. 2012(167). Pp. 1–9. https://ejde.math.txstate.edu/Volumes/2012/167/pisano.pdf

24. Jasinski, R. Validation of elastic-brittle, and elastic-plastic FEM model of the wall made of calcium silicate and AAC masonry units. IOP Conference Series: Materials Science and Engineering. 2019. 603(3). DOI:10.1088/1757-899X/603/3/032001.

25. Červenka, J., Papanikolaou, V.K. Three dimensional combined fracture-plastic material model for concrete. International Journal of Plasticity. 2008. 24(12). Pp. 2192–2220. DOI:10.1016/j.ijplas.2008.01.004. https://www.sciencedirect.com/science/article/pii/S0749641908000259?via%3Dihub.

26. Zhang, J., Ma, L., Zhang, Z.X. Elastoplastic Damage Model for Concrete Under Triaxial Compression and Reversed Cyclic Loading. Strength of Materials. 2018. 50(5). Pp. 724–734. DOI:10.1007/s11223-018-0017-3.

27. Wang, R.Z., Wang, C.Y., Lin, Y.L. Numerical Model of High Strength Concrete. IOP Conference Series: Materials Science and Engineering. 2018. 317(1). DOI:10.1088/1757-899X/317/1/012069.

28. Radosław, J. Identification of the Parameters of Menétrey -Willam Failure Surface of Calcium Silicate Units. IOP Conference Series: Materials Science and Engineering. 2017. 245(3). DOI:10.1088/1757-899X/245/3/032045.

29. Mazzucco, G., Xotta, G., Salomoni, V.A., Majorana, C. Integral-type regularization of non associated softening plasticity for quasi brittle materials. Computers and Structures. 2019. 224. DOI:10.1016/j.compstruc.2019.106120.

30. Pisano, A.A., Fuschi, P., De Domenico, D. Limit state evaluation of steel-reinforced concrete elements by von mises and Meńetrey-Willam-type yield criteria. International Journal of Applied Mechanics. 2014. 6(5). Pp. 1450058. DOI:10.1142/S1758825114500586. https://www.worldscientific.com/doi/pdf/10.1142/S1758825114500586.

31. Pisano, A.A., Fuschi, P., De Domenico, D. Peak loads and failure modes of steel-reinforced concrete beams: Predictions by limit analysis. Engineering Structures. 2013. 56. Pp. 477–488. DOI:10.1016/j.engstruct.2013.05.030. https://www.sciencedirect.com/science/article/pii/S0141029613002538.

32. Pisano, A.A., Fuschi, P., De Domenico, D. A kinematic approach for peak load evaluation of concrete elements. Computers and Structures. 2013. 119. Pp. 125–139. DOI:10.1016/j.compstruc.2012.12.030. https://www.sciencedirect.com/science/article/pii/S0045794913000102.

33. Hokeš, F., Kala, J., Hušek, M., Král, P. Parameter Identification for a Multivariable Nonlinear Constitutive Model inside ANSYS Workbench. Procedia Engineering. 2016. 161. Pp. 892–897. DOI:10.1016/j.proeng.2016.08.743.

34. CEB-FIP Model Code 90. CEB Bulletin. 1993 213/214. Thomas Telford Ltd. ISBN: 978-0-7277-1696-5, London, 460 p. https://www.fib-international.org/publications/ceb-bulletins/ceb-fip-model-code-90-pdf-detail.html

35. fib. Model Code for Concrete Structures 2010. International Federation for Structural Concrete, 2013. ISBN: 978-3-433-03061-5, 434 p.

36. Vermeer, P.A. Non-Associated Plasticity for Soils, Concrete and Rock. Physics of Dry Granular Media. Springer Netherlands. Dordrecht, 1998. Pp. 163–196.

37. Smith, S.S., Willam, K.J., Gerstle, K.H., Sture, S. Concrete over the top, or is there life after peak. ACI Materials Journal. 1989. 86. Pp. 491–497.

38. Frantziskonis, G., Desai, C.S., Somasundaram, S. Constitutive Model for Nonassociative Behavior. Journal of Engineering Mechanics. 1986. 112(9). Pp. 932–946. DOI:10.1061/(ASCE)0733-9399(1986)112:9(932).

39. Hansen, C.E.B. Line ruptures regarded as narrow rupture zones – basic equations based on kinematic considerations. Proc. Brussels Conf. 58 on Earth Pressure Problems. 1958. 1. Pp. 39–48.

40. Rowe, P.W. Theoretical meaning and observed values of deformation parameters for soil. Proc. Rascoe Mem. Symp. on Stress Strain Behaviour of Soils. 1972. Pp. 143–194.

41. Thacker, B.H., Doebling, S.W., Hemez, F.M., Anderson, M.C., Pepin, J.E., Rodriguez, E.A. Concepts of Model Verification and Validation. Technical report, Los Alamos National Lab., Los Alamos, NM, United States. 2004. 28 p. DOI: 10.2172/835920.

42. Oreskes, N., Shrader-Frechette, K., Belitz, K. Verification, Validation, and Confirmation of Numerical Models in the Earth Sciences. Science. 1994. 263(5147). Pp. 641–646. DOI:10.1126/science.263.5147.641. http://science.sciencemag.org/content/263/5147/641.abstract.

43. EN1992-1-1. Eurocode 2: Design of concrete structures - Part 1-1: General rules and rules for buildings. European Committee for Standartization, 2004.

44. Kupfer, H.B., Gerstle, K.H. Behavior of Concrete under Biaxial Stresses. Journal of Engineering Mechanics. 1973. 99. Pp. 853–866.

45. SP 15.13330.2012 Masonry and reinforced masonry structures. Updated edition of SNiP II-22-81*. Ministry of Regional Development of the Russian Federation. Moscow, 2012.

46. Abdel-kareem, A.H., Debaiky, A.S., Makhlouf, M.H., Badwi, M. Repairing and Strengthening of RC Beams using thin Lower Concrete Layer Reinforced by FRP Bars. International Journal of Civil Engineering and Technology. 2019. 10(2). Pp. 1949–1966.

47. Meyer, R., Ahrens, H., Duddeck, H. Material Model for Concrete in Cracked and Uncracked States. Journal of Engineering Mechanics. 1994. 120(9). Pp. 1877–1895. DOI:10.1061/(ASCE)0733-9399(1994)120:9(1877).

48. Němeček, J., Padevět, P., Patzák, B., Bittnar, Z. Effect of transversal reinforcement in normal and high strength concrete columns. Materials and Structures. 2005. 38(7). Pp. 665. DOI:10.1007/BF02484311.

49. Boulifa, R., Samai, M.L., Benhassine, M.T. A new technique for studying the behaviour of concrete in shear. Journal of King Saud University - Engineering Sciences. 2013. 25(2). Pp. 149–159. DOI:10.1016/J.JKSUES.2012.07.001. https://www.sciencedirect.com/science/article/pii/S1018363912000293?via%3Dihub .

50. French, R., Maher, E., Smith, M., Stone, M., Kim, J., Krauthammer, T. Direct shear behavior in concrete materials. International Journal of Impact Engineering. 2017. 108. Pp. 89–100. DOI:10.1016/J.IJIMPENG.2017.03.027. https://www.sciencedirect.com/science/article/pii/S1018363912000293.

51. Mattock, A.H., Hawkins, N.M. Shear transfer in reinforced concrete – recent research. PCI Journal. 1972. 17. Pp. 55–75. DOI:10.15554/pcij.03011972.55.75.